Finite Element Analysis of Tissue Deformation with a Radiofrequency Ablation Electrode for Strain Imaging

Jingfeng Jiang, Tomy Varghese, *Senior Member, IEEE*, Quan Chen, *Student Member, IEEE*, Timothy J. Hall, and James A. Zagzebski, *Associate Member, IEEE*

Abstract—Recent studies have shown that radiofrequency (RF) electrode displacement or deformation-based strain imaging can be used as an alternate imaging modality to monitor and to evaluate ablative therapies for liver tumors. This paper describes a biomechanical model used to study RF electrode deformation-based strain imaging, in conjunction with a simulated medical ultrasound linear array transducer. The computer simulations reported here are important steps toward understanding this biomechanical system *in vivo*, thus providing a basis for improving system design, including the motion tracking algorithm and image guidance for performing RF electrode displacement-strain imaging *in vivo*.

I. Introduction

RADIOFREQUENCY (RF) ablation is a promising technique to treat and destroy tumors in the liver, kidney, and prostate [1]–[6]. This minimally invasive therapy has gained increasing attention in the last decade as an alternative to standard surgical techniques. Continuous monitoring of the tissue damage during and after RF ablation therapy is important to the success of treatment [3], [7]. Unfortunately, conventional ultrasound B-mode images are ineffective at depicting immediate results of treatment as the echogenic properties of tissue do not change significantly during and following ablation to be visualized reliably by the ultrasound imaging system [8]. However, protein denaturation that damages tissue at the molecular level also results in an increase of the tissue modulus [9]. Therefore, ultrasonic elasticity imaging techniques [10]–[12] are useful in monitoring the formation of thermal coagulations. Recent studies have established the feasibility of monitoring these coagulation regions with acoustic radiation-force impulse (ARFI) imaging [13] and strain imaging using the controlled displacement of the RF electrode as the mechanical stimulus [14].

The success of ultrasound-based strain imaging relies on the ability to accurately track *in vivo* tissue motion following tissue deformation. Inducing simple tissue motion (*e.g.*, nearly uniaxial compressions with minimal motion

perpendicular to the ultrasound imaging plane [15]) during deformation would be ideal to achieve the goal. However, controlling the nature of tissue displacements during an externally applied deformation becomes particularly difficult for internal abdominal organs, such as the liver. To overcome this difficulty, Varghese *et al.* [14] proposed an alternative method for deforming tissue during RF ablation, whereby deformations are introduced by the controlled displacement of the RF electrode.

Although the electrode-displacement technique appears to be feasible, as shown in a porcine animal model [14], to date a detailed evaluation of the method has not been performed. The purpose of this paper is to describe a finite-element analysis (FEA)-based biomechanical model that simulates the mechanical response of soft tissues (*e.g.*, liver) to deformations introduced by an RF ablation electrode for strain imaging. Use of the model, in turn, should lead toward improvements and further refinement of this method.

ANSYS, a commercial FEA package (ANSYS Inc., Canonsburg, PA), was used to simulate the deformation of soft tissue under perturbations applied by displacements of the RF ablation electrode. Section II describes how the FEA-based biomechanical model was constructed under relevant hypotheses, including boundary conditions and the representation of thermal lesions (*i.e.*, elasticity distribution) (Table I). We then investigate the difference between a three-dimensional (3-D) FEA model and a simplified 2-D model by comparing FEA model-generated strain images derived from known modulus distributions in computer simulations. The comparisons are based on the contour of the thermally introduced lesion because the boundaries of the lesion appear to provide the most useful information to assess the success or failure of the treatment procedure.

II. Materials and Methods

Varghese *et al.* [14] described the RF electrode displacement method, whereby controllable and reproducible local deformations of tissues near a thermal lesion are introduced for obtaining axial (parallel to the ultrasound beam direction) strain images. In this paper, FEA models are constructed and used to simulate the biomechanical interaction between the RF electrode and surrounding

TABLE I
ANSYS® Finite Elements for our Computer Models and Interested Readers May Consult ANSYS Element Reference for Details.

| FEA Element Type	Description	Modeling
Solid 186	Twenty-node element having three degrees of freedom (3-D) at each node; Solid 186 has quadratic displacement behavior.	Soft tissue (treated and untreated) in 3-D models.
PLANE183	Eight-node element having two degrees of freedom (2-D) at each node; PLANE183 has quadratic displacement behavior; both plane stress and plane strain states were used for computer simulations.	Soft tissue (treated and untreated) in 2-D models.
CONTACT174	Eight-node surface element having three degrees of freedom at each node; CONTACT174 has quadratic displacement behavior and must be paired with its associated "target" surface.	The contact elements overlay the solid elements describing the boundary of relatively rigid RF electrode and are potentially in contact with the interface surface.
TARGET170	Eight-node surface element having three degrees of freedom at each node; TARGET170 has quadratic displacement behavior and must be paired with its associated "contact" surface.	The contact elements overlay the solid elements describing the boundary of deformable soft tissues and are potentially in contact with the interface surface.
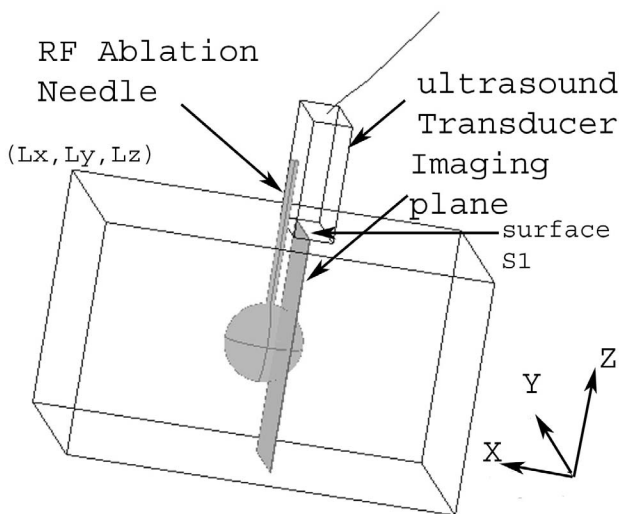
Fig. 1. An illustration of strain-imaging geometry of a typical cool-tip, RF electrode for liver tumor ablation. The surface of the tip is conductive. The electrode can create 20-mm coagulations or thermal lesions. An imaging plane in which RF echo fields are acquired by an ultrasound transducer is 3 mm–5 mm away from the needle electrode.

liver tissue. The FEA simulations are combined with an ultrasound simulation program to produce pre- and post-deformation RF echo fields. From these signals, local strain images are constructed using a 2-D block matching algorithm [16].

Fig. 1 schematically illustrates a typical configuration for data acquisition in which the displacement induced by an RF electrode deforms the tissue. A commonly used, single prong, 1.6-mm diameter electrode (*i.e.*, Valleylab® Cool-tip^TM electrode, Tyco Healthcare Group, Mansfield, MA) insulated both thermally and electrically, except around the 20-mm conducting zone, is simulated in this study.

A. Theory of Finite-Element Simulation

The solution to a conventional continuum mechanics problem using FEA leads to the following linear algebraic system [17]:

$$KU = F, \qquad (1)$$

where K is an assembled global stiffness matrix, U is an assembled global displacement vector, and F is an assembled force vector.

In the framework of contact mechanics, the physical contact can be modeled as interactions among different continua. In general, an admissible solution can be obtained by solving the following constrained optimization problem numerically [17]:

$$\min\{KU - F\} \text{ with } g_N \leq 0, \qquad (2)$$

where physical constraints such as avoiding a collision are described by a set of mathematical functions $g_N \leq 0$.

As illustrated in Fig. 1, the mechanical behavior of an RF ablation electrode-induced displacement is dictated by the contact forces transmitted across the contact layer between the electrode and surrounding tissue. We assume this interaction is governed by Coulomb friction [18]. More specifically, if the shear stress along the contact interface exceeds a predetermined value (*i.e.*, cohesion), the frictional load is proportional through a friction coefficient to the normal pressure applied on the contact surface. Otherwise, there is no relative slippage between the electrode and its surrounding tissue. An integrated environment called "contact wizard" in the ANSYS software was used to handle the interaction between the RF electrode and its surrounding tissue. During a contact analysis, ANSYS checks each element to avoid any potential physical collision. The process is often referred to as the pinball algorithm [19] in which a circular (2-D) or spherical (3-D) region around each potential contact interface is used to make this determination.

In this study, the contribution of the frictional load (excluding the cohesion) is small because the gravity force of any tissue mass is parallel to the friction direction (*i.e.*, the normal pressure acting on the contact interface is small), consistent with our FEA results. Simulations of the deformation field were computed with the friction coefficient varying from 0.05–0.5 to test the sensitivity of this parameter. A friction coefficient of 0.15 is commonly used for an interface between two pieces of lubricated stainless steel [18] and, intuitively, the friction that would exist between the RF electrode and normal *in vivo* tissue will not differ significantly from this value. Our FEA results demonstrate that the strain imaging results were not sensitive to changes in this parameter.

We further hypothesize that protein denaturation and carbonization occurring around the RF ablation electrode tip cause the adhesion of the stainless steel electrode to the ablated tissue [20]. It is logical to assume that no bonding exists (*i.e.*, cohesion = 0) between the electrode and untreated tissue. Different strengths of the bond between the electrode and surrounding tissue can be achieved by varying the cohesion value in ANSYS.

Because geometric (large deformation and large strain) and contact (surface gaps) nonlinearities were included in these simulations, the ANSYS program uses the Newton-Raphson equilibrium iterations [21] to achieve convergence[1]. Convergence to a specific tolerance of 0.1% was used in this study. An interface program was used to read the displacement fields and to convert them into a format that can be read by an acoustic simulation program described below to generate pre- and postdeformation RF echo signals.

B. Three-Dimensional FEA Model

Fig. 1 shows a typical 3-D simulation geometry ($100 \times 100 \times 60$, length $\times$ width $\times$ height in millimeters) in which a single spherical inclusion (Young's modulus of 30 kPa) is used to model an RF ablation-induced lesion embedded in untreated normal liver tissue (Young's modulus of 5 kPa). These Young's modulus values are consistent with experimental results [9]. Normal liver tissue and ablated thermal lesions were assumed to be linearly elastic and nearly incompressible (Poisson's ratio of 0.495). We model the following boundary conditions, assuming that the RF ablation electrode is pulled toward the ultrasound transducer by a fixed displacement increment (*e.g.*, 0.5 mm) under stepper motor control. Because the electrode introduces a small local perturbation, it is reasonable to assume that the motion at the bottom of the tissue is restrained due to anatomical constraints (*e.g.*, connective vessels) and the inertia of the organ being imaged, consistent with our experimental observations. Expressed in an analytical form, this can be written as $u_z = 0$ on the tissue surface defined by $Z = 0$. We also assume that the center point of

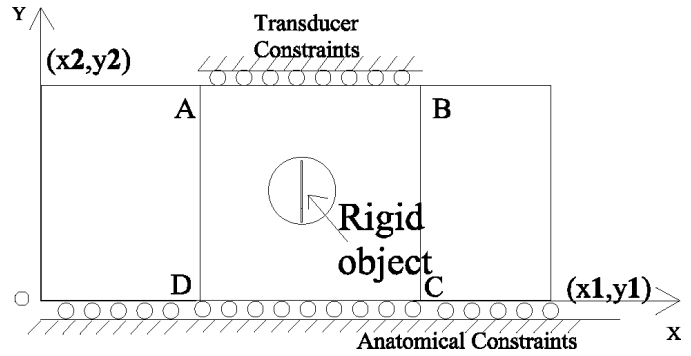[1]ANSYS Theory Reference Manual, 2004 (ANSYS Inc., Canonsburg, PA).

Fig. 2. The 2-D simplified mechanical model for generating RF ablation-induced displacements. Points D and B correspond to (0, 0) and (40, 60), respectively.

the tissue surface at $Z = 0$ is constrained along the X and Y directions to prevent rigid body motion. When tissue is pulled toward the ultrasound transducer (Fig. 1), the transducer limits the tissue motion in the Z direction. Thus, $u_z = 0$ on the contact surface S_1 of the transducer. The friction coefficient used was 0.15, and perfect bonding between the electrode and the treated tissue was assumed.

C. Two-Dimensional Simplified FEA Model

A simplified 2-D model applicable to both plane stress and plane strain boundary conditions is illustrated in Fig. 2 (image plane of 100×60, width $\times$ height in millimeters). In a clinical setting, an ultrasound transducer may be displaced (*e.g.*, 3 mm–5 mm) from the plane of the RF ablation electrode (Fig. 1). Therefore, it is reasonable to treat the deformation source in an image plane as an embedded and finite-sized (width = 1 mm) rigid body along the central line of the lesion, as illustrated in Fig. 2.

Similar boundary conditions were used for the 2-D model as in the 3-D model described above. The bottom boundary ($Y = 0$ in Fig. 2) was taken as being constrained by anatomic confinement and the inertia of the organ; the boundaries of the left and right sides were free. Similarly, the tissue motion around the top boundary [$Y = 60$ mm in Fig. 2(a)] also was limited to simulate confinement of tissue motion provided by the ultrasound transducer when the ablation electrode was displaced toward the transducer.

Three different soft tissue modulus distributions, including representations for the thermally induced lesion and for the untreated region, were simulated for the 2-D FEA model as follows. In the first case, a uniformly elastic phantom (5 kPa approximating that of normal liver tissue) was simulated. This phantom did not contain a circular thermal lesion. In the second case, a phantom containing a 20-mm diameter inclusion was presented. The background modulus is 5 kPa and the inclusion modulus is 30 kPa (approximately that of thermal lesions in normal liver tissue [9]). In the third case, a three-layered, concentric thermal lesion model that incorporates likely characteristics of thermal lesions also was simulated in a phantom. Similarly, the background normal liver tissue is 5 kPa, but

the thermal lesion contains three distinct zones [22]. The region most distant from the electrode is an area of partial necrosis and hemorrhage (2-mm thick in this study) containing some viable cells. The swelling of tissue and increase in fluid content in this zone results in softening of tissue (compared to the untreated tissue) and, therefore, Young's modulus of this zone was assigned to 2 kPa (based on conjecture). The most inner zone (8 mm in diameter) corresponds to a region of completely ablated tissue in which tissues sustain the highest temperature (*e.g.*, > 80°C), and 100% of the cells have been destroyed. The middle zone is completely necrosed, but it is ablated at a relatively lower temperature (*e.g.*, 60°C). The Young's modulus of treated tissue is likely proportional to the ablation temperature [9], [23], [24]. Therefore, we used 30 kPa for the inner zone and 25 kPa for the middle zone [9]. Note that all modulus changes between the two different regions described above are modeled as step functions.

To study the sensitivity of the bond strength between the electrode and the treated tissue on the thermal lesion visibility, the cohesion value was varied from 10 kPa to 1 MPa, while keeping the friction coefficient at 0.15.

D. Ultrasound Simulation Software

Ultrasonic echo data was simulated following a simple linear system approach [25]. The pre- and postdeformation RF echo signals in a coordinate system (x, y) can be expressed as:

$$r_i(x, y) = h(x, y) \otimes z_i(x, y) + n_i(x, y), \qquad (3)$$

where r is the RF echo signal consisting of a set of A-lines, h is the system point spread function (PSF), z is the acoustic impedance difference of tissue modeled by a 2-D Gaussian random field, and n is the signal-independent, zero-mean Gaussian noise. The subscript i in (3) corresponds to pre- (0) and postdeformation (1) data. The postdeformation acoustic field $z_i(x, y)$ is obtained by resampling $z_0(x, y)$ at the new spatial position (x', y'), where $x' = x + dx$, $y' = y + dy$, and (dx, dy) is the displacement field obtained with FEA simulation. The 2-D PSF $h(x, y)$ is modeled axially as a Gaussian-modulated sinusoid and laterally as a Gaussian envelope [25]. The simulated acoustic pulse has a center frequency of 7.5 MHz with a 60% fractional bandwidth. The axial and lateral PSF dimensions (full width at half maximum) were 0.5 mm and 1.2 mm, respectively. Zero-mean Gaussian white noise was added to obtain an electronic signal-to-noise (SNR) of 40 dB. These parameters are typical of modern high end clinical scanners.

E. Data Processing

The data processing strategy (Fig. 3) is similar to conventional approaches to elasticity imaging. The axial displacements from the numerical phantom were estimated using a speckle tracking algorithm [16].
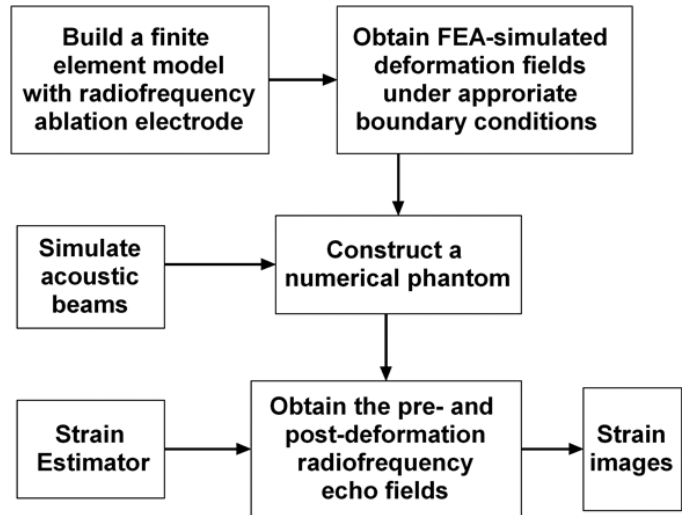

Fig. 3. A block diagram of the procedures for the computer simulations. The computer model consists of both simulations for acoustic beams and representations for mechanical interactions between the RF ablation electrode and its surrounding soft tissues.

This algorithm is a block-matching-based algorithm in which each search kernel consists of a short axial length of echo data from several beam lines (described below). It uses a strategy of a predictive search to achieve real-time performance, similar to a previously published algorithm [26]. In Zhu and Hall's algorithm [26], an estimated displacement vector in one spatial location can be used to guide speckle tracking in the immediate neighborhood because of the continuity of tissue motion. Limiting the search region improves computational efficiency while eliminating phase ambiguity errors in the displacement estimation. Rather than the row-by-row guidance for displacement estimation in Zhu and Hall's algorithm [26], here we use a column-based guidance (column direction is parallel to the acoustic beam direction). A column of high quality displacement vectors is estimated near the center of the region of interest (ROI). Because the column direction is consistent with the applied deformation direction, and axial displacements along a column are larger in magnitude than across a row, local errors in the displacement estimation are more easily detected and corrected in the column direction, resulting in better noise immunity. Then, based on the assumption of motion continuity, displacement estimation among adjacent A-lines can be performed in a significantly reduced region guided by the first column of displacement vectors and its successors [25].

In this study, a small 2-D kernel (0.96 mm × 0.40 mm) is used to obtain the displacement estimates. Axial strain is estimated from the slope of a linear regression of the estimated displacement vectors at the center of a small segment (2.0 mm window).

III. Results

Figs. 4(a)–(c) show the axial strain fields generated using the FEA simulation of a single thermal lesion (*i.e.*, the
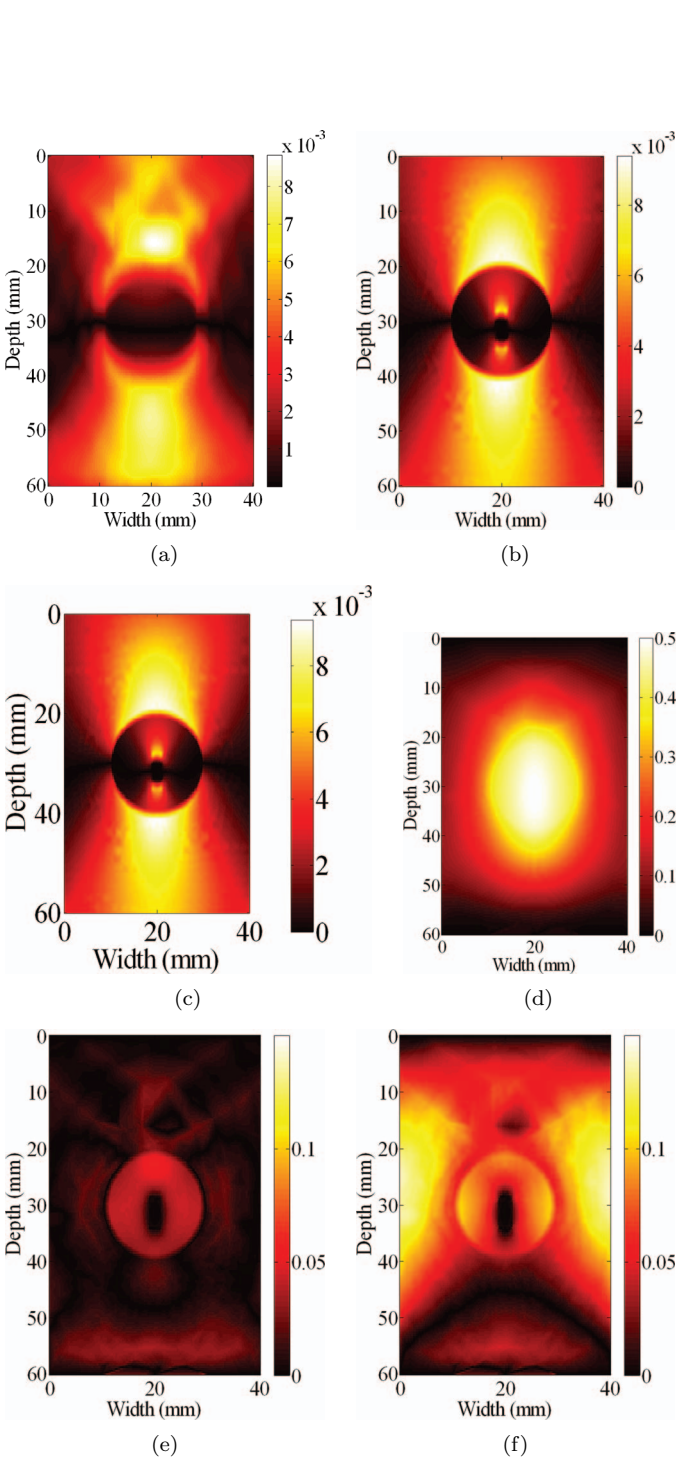
Fig. 4. Axial strain fields (a)–(c) for the true 3-D FEA simulation and two cases of 2-D approximation (plane stress and plane strain states): axial strain fields from (a) 3-D, (b) plane stress, and (c) plane strain. (d) Axial displacement (mm) field from the 3-D simulation and axial displacement difference (mm) images. (e) Between the 3-D and plane stress. (f) Between the 3-D and plane strain.
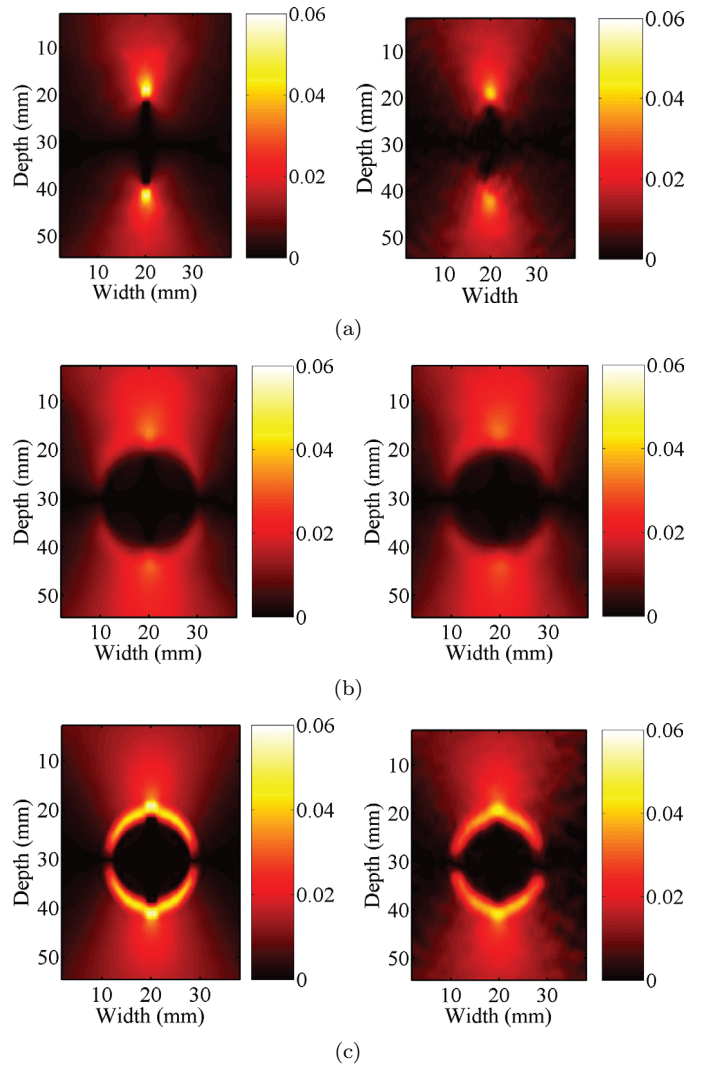

Fig. 5. FEA simulated (left) and estimated (right) strain images for different modulus distributions. (a) Uniform phantom having no thermal lesion. (b) Phantom containing a uniform (30 kPa) thermal lesion. (c) Phantom with a thermal lesion having a layered modulus distribution.

model illustrated in Section II-B versus the second modulus distribution in Section II-C) under true 3-D mechanical conditions, 2-D plane stress and plane strain states, respectively. Observe from Figs. 4(a)–(c), that the 2-D simplification captures the general characteristics (in particular, the lesion contour) of the axial strain induced by the RF ablation electrode. However, there are quantitative differences in the displacement distribution predicted by the 2-D and 3-D models [Figs. 4(e) and (f)]. These differences were computed by comparing axial displacements [see Fig. 4(d)] in an image plane 5 mm away from the electrode in the 3-D FEA simulation to those obtained using 2-D simulations under similar conditions, respectively. For the purpose of visualizing the boundary of a thermally induced lesion, the 2-D FEA model significantly reduces the modeling and computational burden (a few seconds versus many hours) and is, therefore, an appropriate approximation, if it is suf-
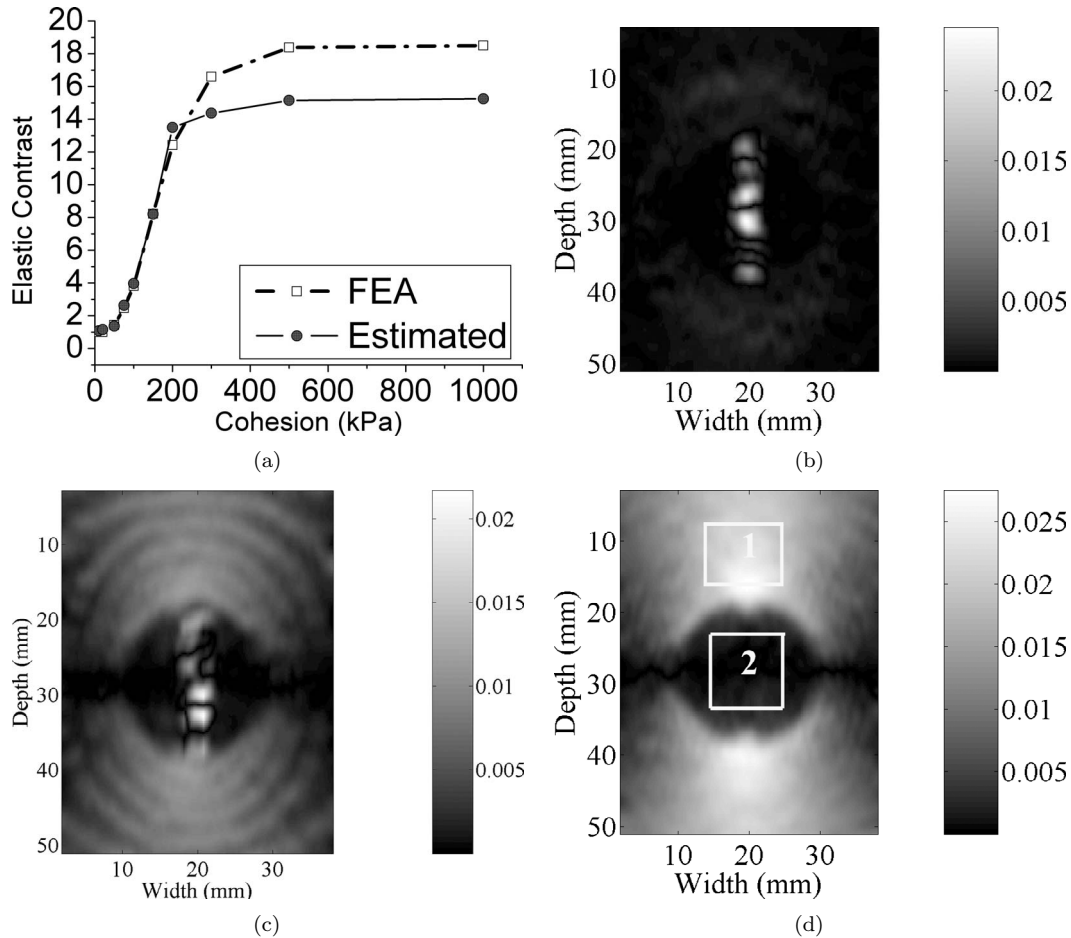
Fig. 6. (a) A plot of estimated elastic contrast with respect to different bonding strengths between the electrode and the treated tissue and corresponding strain images for the second modulus distribution in Section II-C. Bond strength of (b) 10 kPa, (c) 75 kPa, and (d) 200 kPa. The electrode was pulled 0.5 mm toward the transducer, and the elastic contrast was estimated by (the mean strain of region 1)/(the mean strain of region 2).

ficiently accurate. Note that, in all 2-D simulations shown in Fig. 4, perfect bonding between the electrode and the treated tissue was assumed.

The absolute displacement estimates using the 2-D simplification results in errors. The maximum error for the 2-D simplification with the plane stress condition [Fig. 4(e)] is approximately 12%; the 2-D simplification with the plane strain condition [Fig. 4(f)] results in a maximum error of about 30%. Based on the smaller errors, 2-D simplification with the plane stress condition was adopted for the following investigations.

Figs. 5(a)–(c) show the 2-D plane stress FEA simulated (left plots) and estimated (right plots) strain images obtained by the procedure described in Section II-E. Results are shown for three different simulated tissue-mimicking phantoms [no lesion Fig. 5(a), uniform lesion Fig. 5(b), and concentric layered lesion Fig. 5(c)]. Strain images obtained from both FEA simulation and speckle tracking correlate well with the known modulus distributions in the phantom, except for results with the uniform phantom. Even though no elasticity contrast exists in the uniform phantom, the presence of the stainless steel needle electrode in the imaging plane causes rigid body motion (relative to tis-

sue deformation). In other words, the low strain region obtained for the uniform phantom is mainly an artifact that represents the rigid-body motion of the tissue attached to the RF ablation electrode. For the other two thermal lesion models (uniform lesion model and layered lesion model), the circular strain patterns in Figs. 5(b) and (c) are remarkably similar in appearance to electrode-deformation images produced in tissue. Nevertheless, a relatively bright ring that corresponds to the soft zone in the layered lesion model is highly visible in Fig. 5(c). All strain images in Fig. 5 were obtained under perfect bonding conditions between the electrode and treated tissue.

Fig. 6(a) shows the elastic contrasts in the simulated phantom identical to that presented in Fig. 5(b) with respect to different bonding strengths between the electrode and treated tissue. The elastic contrast was estimated by computing the ratio between the mean strains of region 1 and region 2 [see Fig. 6(d)]. The estimated elastic contrast is primarily used as an index of lesion visibility and may be biased due to the strain concentration artifact. When the bonding between the electrode and the treated tissue is weak (cohesion = 10 kPa), no elastic contrast other than the decorrelation artifacts induced by the rigid body mo-

tion of the electrode is observed in Fig. 6(b). After a moderate bonding (cohesion = 75 kPa) is established, the thermally induced lesion is clearly identified in the strain image [see Fig. 6(c)]. If the bond is strong (cohesion = 200 kPa), a high contrast lesion is clearly visualized [see Fig. 6(d)].

IV. DISCUSSION

The motion of the electrode introduces a local perturbation (displacement) of tissues surrounding the electrode. This displacement pattern is significantly different from those used in traditional elastographic imaging in which the deformation stimulus is applied externally using a compression plate or the ultrasound transducer surface. For instance, axial displacements induced by the RF ablation electrode and transferred to the surrounding tissue weaken with increasing distance from the needle [see Fig. 4(d)]. Two 2-D FEA simulated shear strain images under the RF electrode perturbation (pulling 0.5 mm upward; frame-average axial strain is roughly 1%) and the conventional compression technique (1% of uniaxial compression by an ultrasound transducer) are shown in Fig. 7(a)–(b), respectively, for comparison. The deformation in tissue induced by the electrode is primarily transferred through the shear stress along the interface between the electrode and the treated tissue. Therefore, large shear strains can be seen around the electrode in Fig. 7(a); the shear strains in the conventional compression are small under a relatively uniform compression [see Fig. 7(b)]. In addition, little contrast exists in axial strain images obtained under the electrode deformation [see Fig. 5(b)] at points corresponding to the lateral margins of thermal lesions in which local shear deformations prevail [see Fig. 7(a)].

Our primary hypothesis in the use of the RF electrode to provide controlled perturbation of tissue is that ablated tissue is firmly attached (cohesion > 75 kPa) to the electrode, but untreated tissue is not. If the ablated tissue is not firmly bound (cohesion = 10–50 kPa) to the electrode, the electrode easily can be pulled out or pushed in providing very little local deformation of the surrounding tissue and very little strain image contrast [see Figs. 6(a)–(c)]. It is worth noting that the firm bond between the electrode and the ablated tissue is consistent with our experimental experience, though carefully designed experimental validation is needed. From our observations in both *in vitro* and *in vivo* experiments [14], the adhesion can sustain small perturbations (*e.g.*, at least 1-mm displacements by pushing or pulling on the electrode), consistent with our hypothesis.

However, if the untreated tissue is firmly attached to the electrode [Fig. 5(a)], the rigid body motion induced by the electrode is clearly visible and does not correlate well with its modulus distribution, consistent with a theoretical analysis by Barbone and Bamber [27]. This situation likely occurs at the very early stage of RF ablation therapy in which the thermal lesion is small and the bond between the electrode and its surrounding tissue has been weakly established. However, the rigid body artifact only
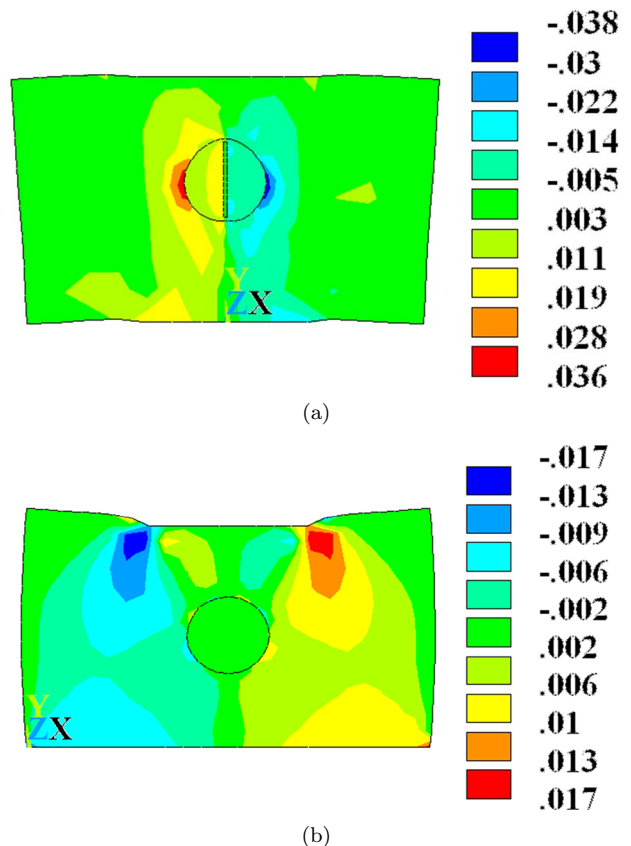

(a)

(b)

Fig. 7. FEA simulated shear strain images induced by (a) a RF electrode (pulling the electrode 0.5 mm upward), and (b) an 1% compression by the ultrasound transducer surface for an simulated phantom (*i.e.*, the second modulus distribution in Section II-C).

will introduce a false target (approximately 3–5 mm wide but 20 mm long [see Fig. 5(a)]) and, therefore, has minimal impact on the visibility of large (> 1 cm) targets [see Figs. 5(b)–(c)]. This topic deserves further consideration in a carefully controlled experimental study.

In this study, the motion induced by pulling or pushing the RF electrode is assumed to be parallel to the transducer axis and represents an ideal situation. An angle between the needle and transducer could induce undesirable lateral and elevational tissue motions, affecting the motion tracking accuracy [28], [29]. We also have limited this study to pushing or pulling of the RF electrode because other motion such as twisting the RF electrode is unlikely unless introduced deliberately.

V. CONCLUSIONS

FEA modeling was used to illustrate the characteristics of axial strain images of thermal lesions obtained by controlled motion of the RF ablation electrode. Strain images of computer simulated phantoms are similar to those generated in *in vivo* experiments [14]. When the RF electrode is tightly bonded with the treated tissue and not bound to the untreated tissue, the size of lesions shown in strain images match well with the known modulus distri-

bution. Several challenges remain, but RF ablation electrode strain imaging appears to be feasible for monitoring ablation therapy in abdominal tissues.

ACKNOWLEDGMENTS

REFERENCES

[1] S. N. Goldberg, G. S. Gazelle, and P. R. Mueller, "Thermal ablation therapy for focal malignancy: A unified approach to underlying principles, techniques, and diagnostic imaging guidance," *Am. J. Roentgenol.*, vol. 174, pp. 323–331, 2000.

[2] J. T. De Sanctis, S. N. Goldberg, and P. R. Mueller, "Percutaneous treatment of hepatic neoplasms: A review of current techniques," *Cardiovasc. Interven. Radiol.*, vol. 21, pp. 273–296, 1998.

[3] S. N. Goldberg, "Radiofrequency tumor ablation: Principles and techniques," *Eur. J. Ultrasound*, vol. 13, pp. 129–147, 2001.

[4] S. Rossi, M. Di Stasi, E. Buscarini, P. Quaretti, F. Garbagnati, L. Squassante, C. T. Paties, D. E. Silverman, and L. Buscarini, "Percutaneous RF interstitial thermal ablation in the treatment of hepatic cancer," *Am. J. Roentgenol.*, vol. 167, pp. 759–768, 1996.

[5] L. Solbiati, T. Ierace, S. N. Goldberg, S. Sironi, T. Livraghi, R. Fiocca, G. Servadio, G. Rizzatto, P. R. Mueller, A. Del Maschio, and G. S. Gazelle, "Percutaneous US-guided radio-frequency tissue ablation of liver metastases: Treatment and follow-up in 16 patients," *Radiology*, vol. 202, pp. 195–203, 1997.

[6] L. Solbiati, S. N. Goldberg, T. Ierace, T. Livraghi, F. Meloni, M. Dellanoce, S. Sironi, and G. S. Gazelle, "Hepatic metastases: Percutaneous radio-frequency ablation with cooled-tip electrodes," *Radiology*, vol. 205, pp. 367–373, 1997.

[7] G. S. Gazelle, S. N. Goldberg, L. Solbiati, and T. Livraghi, "Tumor ablation with radio-frequency energy," *Radiology*, vol. 217, pp. 633–646, 2000.

[8] N. L. Bush, I. Rivens, G. R. ter Haar, and J. C. Bamber, "Acoustic properties of lesions generated with an ultrasound therapy system," *Ultrasound Med. Biol.*, vol. 19, pp. 789–801, 1993.

[9] M. Z. Kiss, T. Varghese, and T. J. Hall, "Viscoelastic characterization of in vitro canine tissue," *Phys. Med. Biol.*, vol. 49, pp. 4207–4218, 2004.

[10] L. Gao, K. J. Parker, R. M. Lerner, and S. F. Levinson, "Imaging of the elastic properties of tissue—A review," *Ultrasound Med. Biol.*, vol. 22, pp. 959–977, 1996.

[11] T. J. Hall, "AAPM/RSNA physics tutorial for residents: topics in US: Beyond the basics: Elasticity imaging with US," *Radiographics*, vol. 23, pp. 1657–1671, 2003.

[12] J. Ophir, S. K. Alam, B. Garra, F. Kallel, E. Konofagou, T. Krouskop, and T. Varghese, "Elastography: Ultrasonic estimation and imaging of the elastic properties of tissues," *Proc. Institution Mech. Eng. Part H—J. Eng. Med.*, vol. 213, pp. 203–233, 1999.

[13] B. J. Fahey, K. R. Nightingale, D. L. Stutz, and G. E. Trahey, "Acoustic radiation force impulse imaging of thermally and chemically induced lesions in soft tissues: Preliminary ex vivo results," *Ultrasound Med. Biol.*, vol. 30, pp. 321–328, 2004.

[14] T. Varghese, J. A. Zagzebski, and F. T. Lee, Jr., "Elastographic imaging of thermal lesions in the liver in vivo following radiofrequency ablation: Preliminary results," *Ultrasound Med. Biol.*, vol. 28, pp. 1467–1473, 2002.

[15] T. J. Hall, Y. Zhu, and C. S. Spalding, "In vivo real-time freehand palpation imaging," *Ultrasound Med. Biol.*, vol. 29, pp. 427–435, 2003.

[16] J. Jiang and T. J. Hall, "A parallelizable real-time ultrasonic speckle tracking algorithm with applications to ultrasonic strain imaging," *Phys. Med. Biol.*, submitted for publication.

[17] R. D. Cook, *Concepts and Applications of Finite Element Analysis: A Treatment of the Finite Element Method as Used for the Analysis of Displacement, Strain, and Stress.* New York: Wiley, 1974.

[18] R. A. Serway, *Physics for Scientists and Engineers.* 3rd ed. Philadelphia: Saunders College Pub., 1990.

[19] T. Belytschko and M. O. Neal, "Contact-impact by the pinball algorithm with penalty and Lagrangian methods," *Int. J. Numer. Methods Eng.*, vol. 31, pp. 547–572, 1991.

[20] T. Mikami, A. Takahashi, K. Hashi, S. Gasa, and K. Houkin, "Performance of bipolar forceps during coagulation and its dependence on the tip material: A quantitative experimental assay," *J. Neurosurg.*, vol. 100, pp. 133–138, 2004.

[21] A. Ralston and P. Rabinowitz, *A First Course in Numerical Analysis.* 2nd ed. New York: McGraw-Hill, 1978.

[22] C. H. Cha, F. T. Lee, Jr., J. M. Gurney, B. K. Markhardt, T. F. Warner, F. Kelcz, and D. M. Mahvi, "CT versus sonography for monitoring radiofrequency ablation in a porcine liver," *Am. J. Roentgenol.*, vol. 175, pp. 705–711, 2000.

[23] W. Tao, J. P. Felmlee, J. F. Greenleaf, S. J. Riederer, and R. L. Ehman, "Assessment of thermal tissue ablation with MR elastography," *Magn. Resonance Med.*, vol. 45, pp. 80–87, 2001.

[24] F. Kallel, R. J. Stafford, R. E. Price, R. Righetti, J. Ophir, and J. D. Hazle, "The feasibility of elastographic visualization of HIFU-induced thermal lesions in soft tissues. Image-guided high-intensity focused ultrasound," *Ultrasound Med. Biol.*, vol. 25, pp. 641–647, 1999.

[25] J. Meunier and M. Bertrand, "Ultrasonic texture motion analysis: Theory and simulation," *IEEE Trans. Med. Imag.*, vol. 14, pp. 293–300, 1995.

[26] Y. Zhu and T. J. Hall, "A modified block matching method for real-time freehand strain imaging," *Ultrason. Imag.*, vol. 24, pp. 161–176, 2002.

[27] P. E. Barbone and J. C. Bamber, "Quantitative elasticity imaging: What can and cannot be inferred from strain images," *Phys. Med. Biol.*, vol. 47, pp. 2147–2164, 2002.

[28] T. Varghese and J. Ophir, "Theoretical framework for performance characterization of elastography: The strain filter," *IEEE Trans. Ultrason., Ferroelect., Freq. Contr.*, vol. 44, pp. 164–172, 1997.

[29] M. Bilgen and M. F. Insana, "Error analysis in acoustic elastography. I. Displacement estimation," *J. Acoust. Soc. Amer.*, vol. 101, pp. 1139–1146, 1997.

Jingfeng Jiang received his B.S. degree in Civil Engineering from the Zhejiang University, China in 1995. He received his M.S. in Computer Science and Ph.D. degree in Civil Engineering from the University of Kansas in 2002 and 2003, respectively. Starting from 2003 he is with the Medical Physics Department at the University of Wisconsin where he is now an assistant scientist and working on algorithm development for elasticity imaging and numerical modeling of biological tissue. His research interests include developing new algorithms for imaging visco-elastic properties of biological tissue and scientific computing.

Tomy Varghese (S'92–M'95–SM'00) is currently an Associate Professor in the Department of Medical Physics at the University of Wisconsin-Madison. He received his Ph.D. in Electrical Engineering from the University of Kentucky, Lexington, KY, in 1995. His current research interests include elastography, ultrasound imaging, ultrasonic tissue characterization, detection and estimation theory, statistical pattern recognition, and signal and image processing applications in medical imaging.

He has worked on developing methods for the visualization of the treated region following radiofrequency ablation using elastographic and temperature imaging methods based on ultrasound. His work in developing ultrasound elastographic imaging techniques and ultrasonic tissue characterization has resulted in over 80 peer-reviewed journal publications, 8 patents, and several presentations in international conferences. Dr. Varghese is a senior member of the IEEE, the American Institute of Ultrasound in Medicine (AIUM), the American Association of Physicists in Medicine (AAPM) and the Eta Kappa Nu.

Quan Chen (S'03) was born in Xinhua, China, in 1975. He received his B.S. degree in physics from Nanjing University, Nanjing, China, in 1996. He spent two years in the Master's program in physics, Southeast University, Nanjing, China, before coming to the United States in 1998. He earned the M.S. and Ph.D. degrees in medical physics in 2000 and 2004, respectively, both from the University of Wisconsin-Madison, Madison, WI. He is currently employed by Tomotherapy Inc., Madison, WI, to develop image processing techniques for image-guided radiation therapy (IGRT).

His research interests include computer modeling in ultrasound, parametric imaging (elastography, scatterer size, and attenuation), and computer vision in medical imaging (including segmentation and deformable registration in ultrasound and CT images).

Timothy J. Hall received his B.A. degree in physics from the University of Michigan-Flint in 1983. He received his M.S. and Ph.D. degrees in Medical Physics from the University of Wisconsin-Madison in 1985 and 1988, respectively. From 1988 to 2002 he was in the Radiology Department at the University of Kansas Medical Center where he worked on measurements of acoustic scattering in tissues, primarily kidneys, on contrast-detail analysis in ultrasound imaging and on developing elasticity imaging techniques including early development of materials for elasticity imaging phantoms. In 2003 he returned to the University of Wisconsin-Madison where he is a Professor in the Medical Physics Department. His research interests continue to center on developing new image formation strategies based on acoustic scattering and tissue viscoelasticty and the development of test objects for system performance evaluation.

James Zagzebski (A'89) was born in Stevens Point, WI in 1944. He received the B.S. degree in physics from St. Mary's College, Winona, MN, and the M.S. degree in physics and the Ph.D. degree in radiological sciences from the University of Wisconsin, Madison. He is a professor of medical physics and of radiology and human oncology at the University of Wisconsin, Madison, WI.

His research interests include ultrasound imaging and tissue characterization, flow detection and visualization using ultrasound, and technological assessment of imaging devices. Dr. Zagzebski's professional affiliations include the IEEE, the American Institute of Ultrasound in Medicine, and the American Association of Physicists in Medicine.